Modified GNSS-PIR and Initial Verifications From the Perspective of Altimetry

Xuebao Hong, Yunlong Zhu, Jie Li, Pengyu Yang, and Dongkai Yang

***Abstract*—This article proposed a modified structure of global navigation satellite system (GNSS) pseudointerferometric reflectometry (GNSS-PIR). The combination of the direct and reflected signals at the front end was modified as the combination of their coherent sums in the baseband so that GNSS-PIR could be more conducive under the framework of conventional GNSS reflectometry. To verify its feasibility, two altimetry experiments were carried out, over land and water surfaces, respectively. Strong oscillations were observed in GNSS-PIR waveforms from both scenes. Altimetry results showed that GNSS-PIR achieved ∼5 cm precision over land surface and ∼4 cm precision over water surface. It indicated that GNSS-PIR was available for retrieving parameters related to reflector height, such as water level and soil moisture.**

***Index Terms*—Altimetry, global navigation satellite system interferometric reflectometry (GNSS-IR), global navigation satellite system pseudointerferometric reflectometry (GNSS-PIR), global navigation satellite system reflectometry (GNSS-R).**

I. INTRODUCTION

GLOBAL navigation satellite system (GNSS) reflectometry (GNSS-R) takes use of the Earth-reflected GNSS signals to retrieve surface geophysical parameters. This technique was first suggested for ocean altimetry by Martín-Neira [1]. And it has been studied as a promising alternative for many remote sensing applications due to its fine temporal–spatial sampling capability at a low cost.

During the past decades, three branches of GNSS-R have been established, including conventional GNSS-R (cGNSS-R), interferometric GNSS-R (iGNSS-R), and GNSS interferometric reflectometry (GNSS-IR). cGNSS-R collects the direct and reflected signals separately, and cross correlates the reflected signal with a local replica of the direct signal to generate the complex field or delay-Doppler map of the reflected signal. It has a wide applicability to ocean and land parameter remote sensing, such as water surface height [2], [3], sea wind speed [4], [5], soil moisture [7], [8], and wetland dynamics [9]. iGNSS-R follows cGNSS-R in signal reception but cross correlates the reflected signal with a compensated direct signal to generate the delay-Doppler map. It is specifically proposed for spaceborne ocean altimetry since the full power spectrum of the transmitted signals can be exploited to significantly improve the code-based height estimation performance [10]. Different from the above two branches, GNSS-IR is developed based on the interference effect between the direct signal and the reflected signal in the ground/shore-based scenario. It utilizes conventional GNSS receivers to obtain the interference patterns, i.e., signal-to-noise ratios of the interference signal, and retrieve environmental parameters by analyzing the oscillating metrics of the patterns. Numerous studies have shown that GNSS-IR is available for soil moisture retrieval [11], [12], [13], snow depth estimation 0, water-level monitoring [15], etc.

In our previous work, we proposed the GNSS pseudointerference reflectometry (GNSS-PIR) for ground-based soil moisture remote sensing [16]. It builds interference patterns under the cGNSS-R architecture and retrieves soil moisture in a GNSS-IR way. To obtain the patterns, the combination of the direct and reflected signals is cross correlated with a local replica of the direct signal. It can achieve higher pattern quality than GNSS-IR, owing to the strong reflected signals ensured by the down-looking antenna, which is helpful to improve retrieval performance. Since combining the signals in the front end is not so conducive, we proposed a modified GNSS-PIR structure. Its feasibility was preliminarily verified from the perspective of altimetry using the data collected over land and water surfaces.

The rest of this article is organized as follows. Section II presents the modified structure of GNSS-PIR. Section III introduces the experimental campaigns. Section IV introduces the data processing methodology and discusses the altimetry results. Finally, Section V concludes this article.

II. MODIFIED GNSS-PIR

As shown in Fig. 1(a), the original GNSS-PIR builds the pseudointerference signal by combining the signal received by an up-looking RHCP antenna and the signal received by a down-looking LHCP antenna in the radio frequency front end of a conventional GNSS-R instrument

$$u_c(t) = u_r(t) + u_l(t) \tag{1}$$

Manuscript received 19 January 2024; revised 22 March 2024; accepted 15 April 2024. Date of publication 19 April 2024; date of current version 25 April 2024. This work was supported in part by the National Key Research and Development Program of China under Grant 2022YFB3904402 and in part by Shanghai Aerospace Science and Technology Innovation Fund under Grant SAST2020-075. *(Corresponding author: Yunlong Zhu.)*

Xuebao Hong was with the Research Institute for Frontier Science, Beihang University, Beijing 100191, China. He is now with the College of Electronic and Information Engineering, Shenyang Aerospace University, Shenyang 110136, China (e-mail: Joyce_hong2008@yeah.net).

Yunlong Zhu, Jie Li, and Pengyu Yang are with the School of Electronic and Information Engineering, Beihang University, Beijing 100191, China (e-mail: zhuyunlong@buaa.edu.cn; Lzzz18@buaa.edu.cn; zy2102418@buaa.edu.cn).

Dongkai Yang is with the School of Electronic and Information Engineering, Beihang University, Beijing 100191, China, also with the International Innovation Institute, Beihang University, Hangzhou 311115, China (e-mail: edkyang@buaa.edu.cn).

Digital Object Identifier 10.1109/JSTARS.2024.3391513

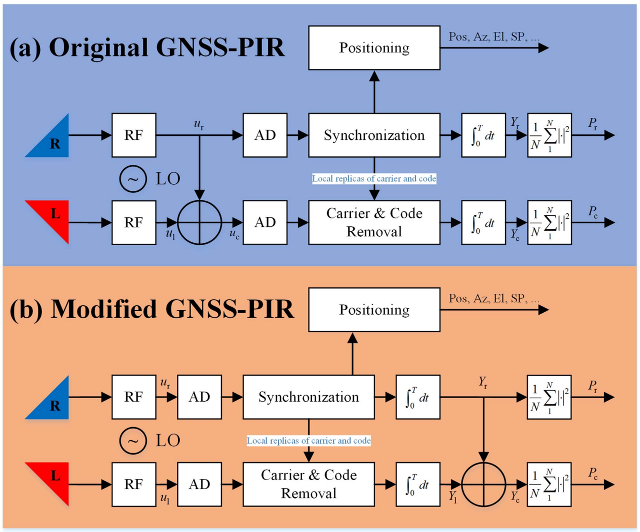

Fig. 1. Signal processing structures of GNSS-PIR. (a) Original GNSS-PIR. (b) Modified GNSS-PIR.

where u_c is the pseudointerference signal; and u_r and u_l are the signals received by the RHCP antenna and the LHCP antenna.

The coherent sum of the pseudointerference signal can be obtained by demodulating and despreading the signal with the local carrier and code replicas of the direct signal

$$Y_c(n) = \frac{1}{T_c}\int_{t_0+(n-1)\cdot T_c}^{t_0+n\cdot T_c} u_c(t)\, a(t) \exp\left[-j\left(2\pi f t + \varphi\right)\right] dt \tag{2}$$

where Y_c is the coherent sum of the pseudointerference signal; t_0 is the start time of the coherent integration; T_c is the coherent integration period; a is the local code replica; and f and φ are the frequency and phase of the local carrier replica.

Substituting (1) into (2), we have

$$\begin{aligned} Y_c(n) &= \frac{1}{T_c}\int_{t_0+(n-1)\cdot T_c}^{t_0+n\cdot T_c} \left[u_r(t) + u_l(t)\right] a(t) \\ &\quad \times \exp\left[-j\left(2\pi f t + \varphi\right)\right] dt \\ &= \frac{1}{T_c}\int_{t_0+(n-1)\cdot T_c}^{t_0+n\cdot T_c} u_r(t)\, a(t) \exp\left[-j\left(2\pi f t + \varphi\right)\right] dt \\ &\quad + \frac{1}{T_c}\int_{t_0+(n-1)\cdot T_c}^{t_0+n\cdot T_c} u_l(t)\, a(t) \exp\left[-j\left(2\pi f t + \varphi\right)\right] dt. \end{aligned} \tag{3}$$

The two integral expressions on the right-hand side are the coherent sums of the signals received by the RHCP antenna and the LHCP antenna, respectively. That is to say, combining the signals in the front-end part is equivalent to combining their coherent sums in the baseband part. As the latter way is more operational, we modify the structure of GNSS-PIR accordingly, as shown in Fig. 1(b).

To simplify the discussion, we assume that the reflector is horizontal and flat, and the antennas only receive the copolarized signals from their forward directions. Then, the received signals can be modeled as follows:

$$\begin{aligned} u_r(t) &= A_r(t)\, D(t)\, C(t) \exp\left[j \cdot \left(2\pi f_0 t + \varphi_0\right)\right] \\ u_l(t) &= A_l(t)\, D(t-\tau)\, C(t-\tau) \exp \\ &\quad \times \left[j \cdot \left(2\pi f_0 t + \varphi_0 + \phi + \Delta\phi\right)\right] \end{aligned} \tag{4}$$

where A represents the signal amplitude; D stands for the navigation bit; C is the PRN code; f_0 and φ_0 are the center frequency and initial phase of the carrier; τ is the delay of the reflected signal with respect to the direct one; $\Delta\phi$ is the phase shift caused by signal reflection; and ϕ is the phase difference between the reflected signal and the direct signal, and it holds

$$\phi = \frac{2\pi}{\lambda}\left(2H + d\right)\sin\theta \tag{5}$$

where λ is the wavelength of the GNSS signal; H is the height of the LHCP antenna; d is the height difference between the two antennas; and θ is the satellite elevation angle.

Then, the coherent sum of the pseudointerference signal can be expressed as follows:

$$\begin{aligned} &Y_c(n) \approx D(n) \\ &\times \left\{A_r(n) + A_l(t) \exp\left[j \cdot \frac{2\pi}{\lambda}\left(2H + d\right)\sin\theta + j \cdot \Delta\phi\right]\right\}. \end{aligned} \tag{6}$$

By integrating the coherent sum incoherently, we can obtain the correlation power of the pseudointerference signal.

$$P_c(n) = \frac{1}{N}\sum_{i=1+(n-1)\cdot N}^{n\cdot N} \left|Y_c(i)\right|^2 \tag{7}$$

where P_c is the correlation power of the pseudointerference signal, and N is the number of incoherently integrated samples.

Finally, the correlation power expression can be written as follows:

$$\begin{aligned} P_c(n) &= {A_r}^2(n) + {A_l}^2(n) + 2A_r(n)\, A_l(n) \\ &\times \cos\left[\frac{2\pi}{\lambda}\left(2H + d\right)\sin\theta + \Delta\phi\right]. \end{aligned} \tag{8}$$

It is an oscillatory sequence with a trend. By extracting the metrics of the oscillation, namely, amplitude, frequency, and phase, we can retrieve environmental parameters using physical or empirical models.

III. EXPERIMENTAL CAMPAIGNS

Two short-term experiments were carried out to verify the feasibility of GNSS-PIR from the perspective of altimetry.

A. Data Acquisition System

An RHCP antenna (5 dBi) and an LHCP antenna (13 dBi) are utilized to receive the direct and reflected GPS $L1$ C/A signals. A dual-channel collector is deployed to record the received signals. It downconverts the signals to 3.996 MHz, samples the signals at a rate of 16.369 MHz, and quantizes the samples into 2-bit raw data. A laptop is used to configure the signal collector, control the data acquisition, and store the raw data.

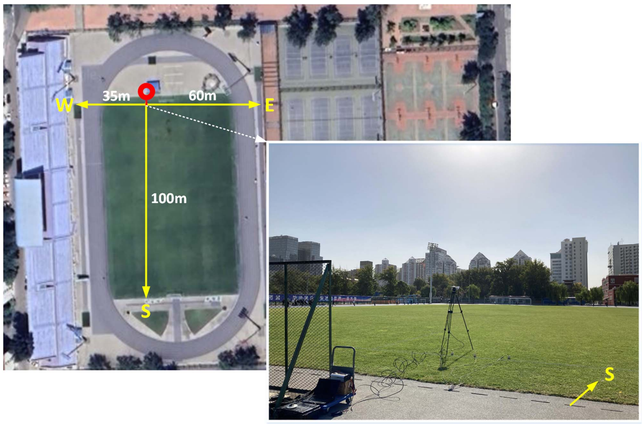

Fig. 2. Scenario of the experiment over land surface.

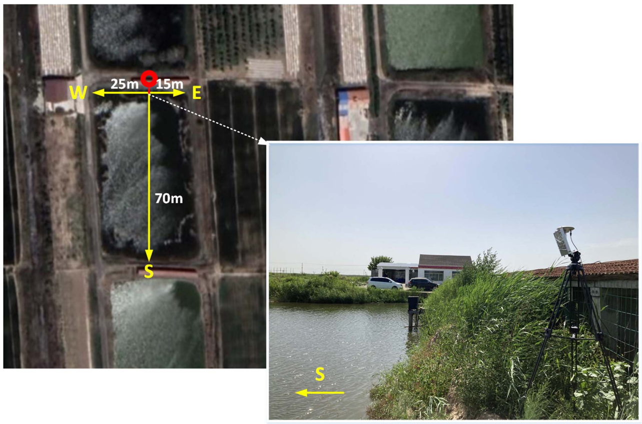

Fig. 3. Scenario of the experiment over water surface.

TABLE I
DATA COLLECTED DURING THE EXPERIMENT OVER LAND SURFACE

Block No.	Y/M/D	Time Period	H (m)	d (m)
1	2020/10/20	20:43–21:56	~1.95	~0.06
2	2020/10/21	10:49–12:16		
3	2020/10/21	12:22–13:54		

TABLE II
DATA COLLECTED DURING THE EXPERIMENT OVER WATER SURFACE

Block No.	Y/M/D	Time Period	H (m)	d (m)
1	2023/07/05	15:24–17:42	~3.18	~0.10
2	2023/07/06	12:13–14:58	~3.03	
3	2023/07/06	15:31–18:16	~2.83	

B. Experiment Over Land Surface

The experiment over land surface was carried out on a football field (39°58′45″ N, 116°20′23″ E) in Beijing, China, on 20th and 21st October 2020. The antennas were installed on the north side of the field. The RHCP antenna looked to the zenith, while the LHCP one pointed to the land surface (∼180° in azimuth with respect to the north, and ∼45° below the horizon). Fig. 2 shows the experimental scenario. Table I presents the data blocks collected during the experiment.

C. Experiment Over Water Surface

The experiment over water surface was carried out beside a fish pond (37°48′52″ N, 118°31′33″ E) in Dongying, China, on 5th and 6th July 2023. The antennas were installed on the north bank of the pond. The RHCP antenna looked to the zenith, while the LHCP one pointed to the water surface (∼180° in azimuth with respect to the north, and ∼65° below the horizon). The experimental scenario is shown in Fig. 3, and the data blocks collected during the experiment are presented in Table II.

IV. DATA PROCESSING AND RESULTS DISCUSSION

A. Data Processing

A GNSS-R software developed based on the GNSS receiver in [17] is used to process the raw signals. It outputs 1-ms complex coherent sums of the signals received by the antennas, as well as elevation and azimuth angles of visible satellites.

With the complex coherent sums, we build 1 s incoherently integrated GNSS-PIR waveforms. Any waveform with nonmonotonic elevation angles has to be divided to ensure that all waveforms have monotonic elevation angles. Then, the data quality control is conducted: First, samples whose azimuth angles do not lie between 90° and 270° are filtered out, as the down-looking antenna faces south during the experiments; second, waveforms that contain less than three periods of oscillations are filtered out since wavenumber affects the accuracy of frequency estimation.

Afterward, we calculate the height of the LHCP antenna according to the following steps:

1) remove the trend from the waveform by variational mode decomposition [18];
2) estimate the spectrum of the detrended waveform with Lomb–Scargle periodogram [19], [20];
3) retrieve antenna height with the peak frequency obtained from the spectrum according to the following formula:

$$H_e = \frac{f_{\mathrm{PIR}}\lambda - d}{2} \tag{9}$$

where H_e is the effective antenna height, and f_{PIR} stands for the oscillation frequency of the GNSS-PIR waveform. For the purpose of comparison, we also build 1 s incoherently integrated GNSS-IR waveforms and estimate the height of the same antenna. The height retrieval formula is given as follows:

$$H_e = \frac{f_{\mathrm{IR}}\lambda}{2} - d \tag{10}$$

where f_{IR} stands for the oscillation frequency of the GNSS-IR waveform.

B. Results Discussion

Figs. 4 and 5 display the specular points of the reflected signals from available satellites and the correlation power waveforms of the interference signals from these satellites obtained in the land surface experiment and the water surface experiment, respectively. It is obvious that both GNSS-IR and GNSS-PIR waveforms possess the characteristics of amplitude-modulated

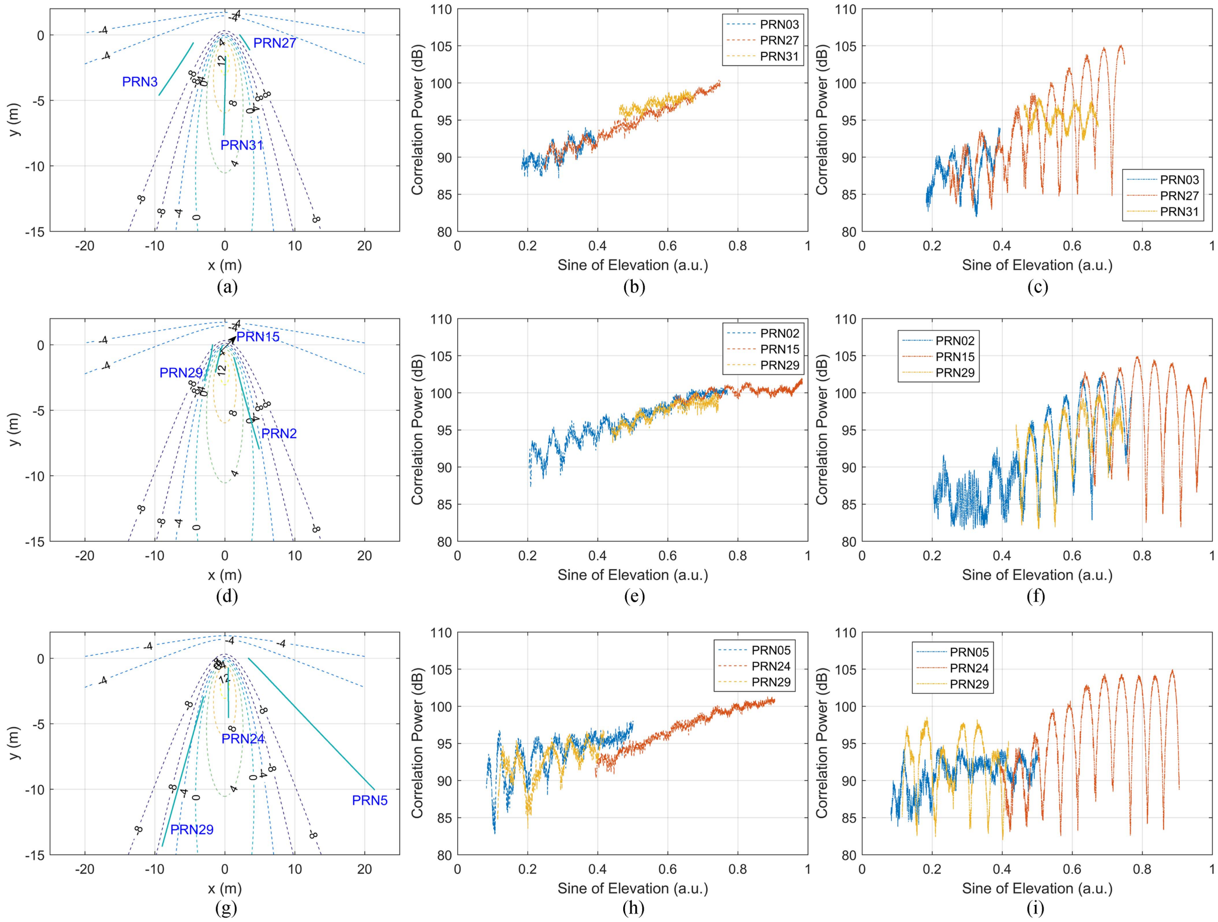

Fig. 4. Specular points and oscillatory waveforms in land surface experiment. (a), (d), and (g) are the specular points of data blocks 1–3; the dotted lines are the contours of LHCP antenna gain. (b), (e), and (h) are the GNSS-IR waveforms of data blocks 1–3. (c), (f), and (i) are the GNSS-PIR waveforms of data blocks 1–3.

sinusoids. The oscillations in GNSS-IR waveforms weaken with the increase of elevation, while those in GNSS-PIR waveforms appear when the specular points of the reflected signals pass through the coverage of the LHCP antenna. And it is remarkable that the waveforms of GNSS-PIR oscillate more intensely than those of GNSS-IR because the reflected signals received by the LHCP antenna are mostly much stronger than those received by the RHCP antenna.

Fig. 6 demonstrates the heights of the LHCP antenna derived from the waveforms. It can be seen that the retrieved results are basically consistent with the reference heights in both scenes. However, it should be mentioned that some PRNs provide height results with large absolute errors (>0.15 m), e.g., PRN03 in data block 1 of the land surface experiment and PRN15 in data block 1 of the water surface experiment. The specular points of these PRNs mainly locate in the southwest/southeast part of the experimental fields. As the fields are not open enough in the east–west direction, it is highly likely that the reflected signals from these PRNs are compromised by the surroundings, e.g., the auditoriums of the football field and the banks of the fish pond. Particularly, GNSS-IR provides more large-error measurements than GNSS-PIR in the water surface experiment. According to the antenna installation, it is reasonable to infer that the low-elevation part of a GNSS-IR waveform contributes the majority to its power spectrum, while it is the medium-elevation part of GNSS-PIR case. As a result, GNSS-IR waveforms are more likely to be affected than those of GNSS-PIR in the water surface case.

TABLE III
ERRORS OF RETRIEVED ANTENNA HEIGHTS

Experiment	Land surface experiment		Water surface experiment	
Method	GNSS-IR	GNSS-PIR	GNSS-IR	GNSS-PIR
MAE(m)	0.130	0.074	0.179	0.039
RMSE(m)	0.139	0.095	0.219	0.062
MAE*(m)	0.107	0.046	0.087	0.027
RMSE*(m)	0.111	0.053	0.088	0.036

To evaluate the overall retrieved results, mean absolute error (MAE) and root-mean-square error (RMSE) are further calculated. As the measurements with large absolute errors contribute significantly to the statistical errors under small sample size condition, we calculate MAE and RMSE in two ways, i.e., with and without (*) the results whose absolute errors are greater than 0.15 m, as presented in Table III.

With large-error measurements, GNSS-PIR performs better in the water surface case than in the land surface case, while

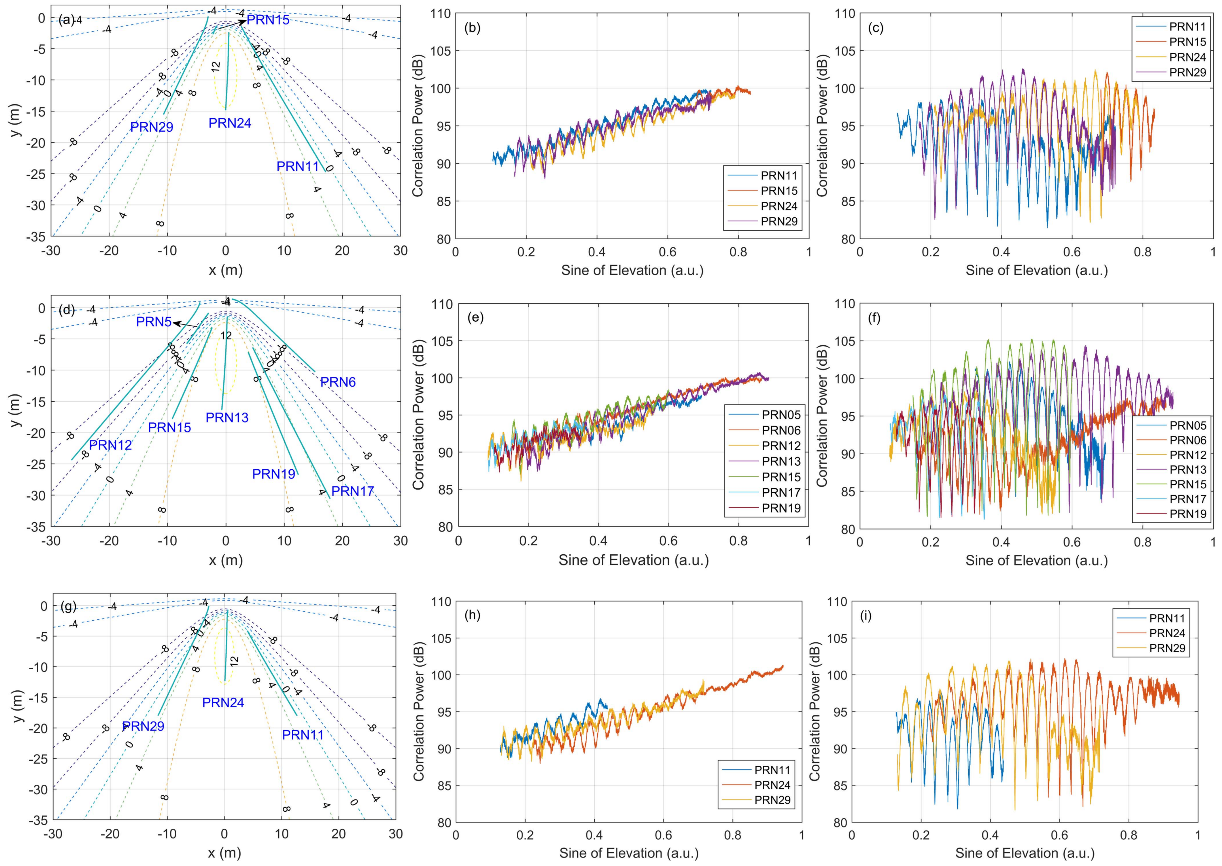

Fig. 5. Specular points and oscillatory waveforms in water surface experiment. (a), (d), and (g) are the specular points of data blocks 1–3; the dotted lines are the contours of LHCP antenna gain. (b), (e), and (h) are the GNSS-IR waveforms of data blocks 1–3. (c), (f), and (i) are the GNSS-PIR waveforms of data blocks 1–3.

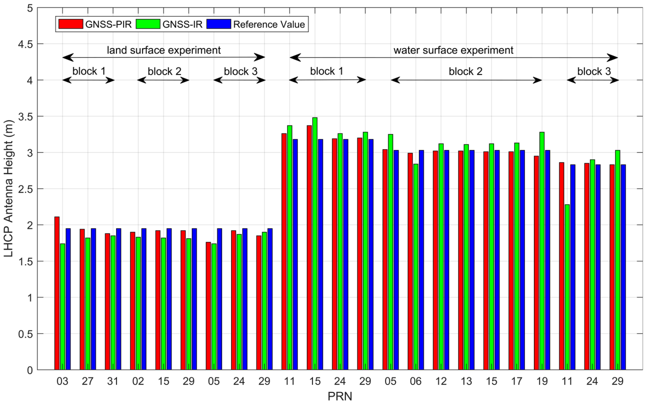

Fig. 6. LHCP antenna heights retrieved in the two experiments.

GNSS-IR performs oppositely. Without large-error measurements, both GNSS-PIR and GNSS-IR perform better in the water surface case than in the land surface case, which is in line with common sense. And it is encouraging that GNSS-PIR achieves lower MAE and RMSE than GNSS-IR in the two experiments. The above analysis indicates that GNSS-PIR is feasible for ground/shore-based altimetry, and there is a strong possibility that GNSS-PIR performs better than GNSS-IR, at least in the scenes which are of limited openness.

V. CONCLUSION

In this work, we modified the structure of GNSS-PIR so that it could be easily realized under the framework of cGNSS-R. And we carried out two ground-based experiments, one over land surface and the other one over water surface, to evaluate the feasibility of GNSS-PIR from the perspective of altimetry. Strong oscillations were observed in the GNSS-PIR correlation power waveforms when the specular points of the reflected signals passed through the coverage of the down-looking LHCP antenna. The experimental results showed that GNSS-PIR was feasible for altimetry and achieved better accuracy than GNSS-IR. It indicates that GNSS-PIR has the potential to be used in the applications related to reflector height retrieval, such as water-level monitoring, snow depth estimation, and soil moisture observation, especially in the scenes, which are not open enough. Next, we will focus on long-term validations for GNSS-PIR in specific applications.

REFERENCES

[1] M. Martín-Neira, “A passive reflectometry and interferometry system (PARIS): Application to ocean altimetry,” *ESA J.*, vol. 17, no. 4, pp. 331–355, Dec. 1993.

[2] J. Zhang and Y. J. Morton, “Inland water body surface height retrievals using CYGNSS delay Doppler maps,” *IEEE Trans. Geosci. Remote Sens.*, vol. 61, Nov. 2023, Art. no. 4209316.

[3] E. Cardellach et al., "First precise spaceborne sea surface altimetry with GNSS reflected signals," *IEEE J. Sel. Topics Appl. Earth Observ. Remote Sens.*, vol. 13, pp. 102–112, Feb. 2020.

[4] W. Li et al., "Initial results of typhoon wind speed observation using coastal GNSS-R of BeiDou GEO satellite," *IEEE J. Sel. Topics Appl. Earth Observ. Remote Sens.*, vol. 9, no. 10, pp. 4720–4729, Oct. 2016.

[5] T. Qiu et al., "Retrieving ocean surface wind speeds in real time on spaceborne GNSS-R receivers: Algorithm and validation," *IEEE J. Sel. Topics Appl. Earth Observ. Remote Sens.*, vol. 17, pp. 2201–2212, Jan. 2024.

[6] M. Asgarimehr, C. Arnold, T. Weigel, C. Ruf, and J. Wickert, "GNSS reflectometry global ocean wind speed using deep learning: Development and assessment of CyGNSSNet," *Remote Sens. Environ.*, vol. 269, Feb. 2022, Art. no. 112801.

[7] W. Ban, K. Yu, and X. Zhang, "GEO-satellite-based reflectometry for soil moisture estimation: Signal modeling and algorithm development," *IEEE Trans. Geosci. Remote Sens.*, vol. 56, no. 3, pp. 1829–1838, Mar. 2018.

[8] O. Eroglu, M. Kurum, D. Boyd, and A. C. Gurbuz, "High spatio-temporal resolution CYGNSS soil moisture estimates using artificial neural networks," *Remote Sens.*, vol. 11, no. 19, Sep. 2019, Art. no. 2272.

[9] M. Morris, C. Chew, J. T. Reager, R. Shah, and C. Zuffada, "A novel approach to monitoring wetland dynamics using CYGNSS: Everglades case study," *Remote Sens. Environ.*, vol. 233, Nov. 2019, Art. no. 11417.

[10] M. Martin-Neira, S. D'Addio, C. Buck, N. Floury, and R. Prieto-Cerdeira, "The PARIS ocean altimeter in-orbit demonstrator," *IEEE Trans. Geosci. Remote Sens.*, vol. 49, no. 6, pp. 2209–2237, Jun. 2011.

[11] K. M. Larson, E. E. Small, E. D. Gutmann, A. Bilich, P. Axelrad, and J. Braun, "Using GPS multipath to measure soil moisture fluctuations: Initial results," *GPS Solutions*, vol. 12, no. 3, pp. 173–177, Jul. 2008.

[12] M. M. El Hajj et al., "Ground-based soil moisture retrieval using the correlation between dual-polarization GNSS-R interference patterns," *IEEE Trans. Geosci. Remote Sens.*, vol. 62, 2024, Art. no. 5800210.

[13] N. Roussel et al., "Detection of soil moisture variations using GPS and GLONASS SNR data for elevation angles ranging from 2° to 70°," *IEEE J. Sel. Topics Appl. Earth Observ. Remote Sens.*, vol. 9, no. 10, pp. 4781–4794, Oct. 2016.

[14] F. G. Nievinski and K. M. Larson, "Inverse modeling of GPS multipath for snow depth estimation—Part II: Application and validation," *IEEE Trans. Geosci. Remote Sens.*, vol. 52, no. 10, pp. 6564–6573, Oct. 2014.

[15] T. S. Dahl-Jensen, O. B. Andersen, S. D. P. Williams, V. Helm, and S. A. Khan, "GNSS-IR measurements of inter annual sea level variations in Thule, Greenland from 2008–2019," *Remote Sens.*, vol. 13, no. 24, Dec. 2021, Art. no. 5077.

[16] X. Hong, B. Zhang, A. Geiger, M. Han, and D. Yang, "GNSS pseudo interference reflectometry for ground-based soil moisture remote sensing: Theory and simulations," *IEEE Geosci. Remote Sens. Lett.*, vol. 19, Jan. 2022, Art. no. 8003705.

[17] K. Borre, D. M. Akos, N. Bertelsen, P. Rinder, and S. H. Jesen, *A Software-Defined GPS and Galileo Receiver: A Single-Frequency Approach*. Berlin, Germany: Springer, 2007.

[18] K. Dragomiretskiy and D. Zosso, "Variational mode decomposition," *IEEE Trans. Signal Process.*, vol. 62, no. 3, pp. 531–544, Feb. 2014.

[19] N. R. Lomb, "Least-squares frequency analysis of unequally spaced data," *Astrophys. Space Sci.*, vol. 39, pp. 447–462, 1976.

[20] J. D. Scargle, "Studies in astronomical time series analysis: II—Statistical aspects of spectral analysis of unevenly spaced data," *Astrophysical J.*, vol. 263, pp. 835–853, 1982.

Xuebao Hong received the B.S. degree in electronic and information engineering and the Ph.D. degree in communication and information systems from Beihang University, Beijing, China, in 2012 and 2021, respectively.

From 2021 to 2023, he was a Postdoctoral Fellow with the Research Institute for Frontier Science, Beihang University. Since 2024, he has been a Lecturer with the College of Electronic and Information Engineering, Shenyang Aerospace University, Shenyang, China. His research interests include GNSS reflectometry and its land remote sensing applications.

Yunlong Zhu received the B.S. degree in information engineering from Beijing Information Science and Technology University, Beijing, China, in 2001, and the Ph.D. degree in signal and information processing from Beihang University, Beijing, in 2011.

From 2012 to 2014, he was a Postdoctoral Fellow with Beihang University. Since 2014, he has been a Lecturer with the School of Electronic and Information Engineering, Beihang University. His research interests include GNSS SAR.

Jie Li received the B.S. degree in communication engineering and M.S. degree in communication and information engineering from the Institute of Technology, Harbin, China, in 2016 and 2018, respectively. He is currently working toward the Ph.D. degree in communication and information systems with Beihang University, Beijing, China.

His research interests include GNSS reflectometry for land applications.

Pengyu Yang received the B.S. degree in communication engineering from the Tiangong University, Tianjin, China, in 2021. He is currently working toward the M.S. degree in communication engineering with Beihang University, Beijing, China.

His research interests include GNSS reflectometry altimetry.

Dongkai Yang received the B.S. degree in electronic engineering from the North University of China, Taiyuan, China, in 1994, and the M.S. and Ph.D. degrees in communication and information system from Beihang University, Beijing, China, in 1997 and 2000, respectively.

From 2001 to 2002, he was a Research Fellow with Nanyang Technological University, Singapore. Since 2010, he has been a Full Professor with the School of Electronic and Information Engineering, Beihang University. His research interests include GNSS and its applications.